Computer Physics Communications 183 (2012) 2128–2135

Contents lists available at SciVerse ScienceDirect

Computer Physics Communications

journal homepage: www.elsevier.com/locate/cpc

# Finite difference discretization of semiconductor drift-diffusion equations for nanowire solar cells

Alexei Deinega *, Sajeev John

*Department of Physics, University of Toronto, 60 St. George Street, Toronto, Ontario, Canada M5S 1A7*

ARTICLE INFO

*Article history:*
Received 22 November 2011
Accepted 16 May 2012
Available online 23 May 2012

*Keywords:*
Nanowires
Nanorods
Finite difference
Radial finite difference

ABSTRACT

We introduce a finite difference discretization of semiconductor drift-diffusion equations using cylindrical partial waves. It can be applied to describe the photo-generated current in radial pn-junction nanowire solar cells. We demonstrate that the cylindrically symmetric ($l = 0$) partial wave accurately describes the electronic response of a square lattice of silicon nanowires at normal incidence. We investigate the accuracy of our discretization scheme by using different mesh resolution along the radial direction $r$ and compare with 3D $(x, y, z)$ discretization. We consider both straight nanowires and nanowires with radius modulation along the vertical axis. The charge carrier generation profile inside each nanowire is calculated using an independent finite-difference time-domain simulation.



The drift-diffusion model for photo-generated electrons and holes is widely used for semiconductor device and solar cell simulations. This model is defined by Poisson and continuity equations [1]:

$$\nabla^2\psi = -\frac{q}{\varepsilon}(p - n + N_D - N_A), \tag{1}$$

$$\nabla J_n = -\nabla J_p = q(R - G), \tag{2}$$

$$J_n = qD_n\nabla n - q\mu_n n\nabla\psi, \tag{3}$$

$$J_p = -qD_p\nabla p - q\mu_p p\nabla\psi, \tag{4}$$

where $\psi$ is the electrostatic potential, $q$ is the elementary electronic charge, $\varepsilon$ is the dielectric function, $n$ and $p$ are the electron and hole densities, $N_D$ and $N_A$ are the concentrations of ionized donors and acceptors, $R$ and $G$ are the recombination and generation rates, and $J_i$, $D_i$ and $\mu_i$ are the current densities, diffusion coefficients and mobilities, $i = n, p$.

Numerical solution of these equations is commonly implemented using finite difference, finite boxes or finite element methods [2,3]. The finite difference method is the simplest to implement. It is very stable and leads to a system of nonlinear equations with simple Jacobian structure that can be efficiently solved by Newton's technique [2,3]. However, this method is less flexible in varying of mesh resolution and mesh alignment with non-planar boundaries. Semiconductor structures comprised of cylindrical nanowires are one example of this situation. Some finite boxes or finite element techniques, exploiting the rotational symmetry of such structures, have been implemented in available simulators [4–6].

In this work we present a simple finite difference scheme adapted for structures with nearly cylindrical symmetry. We demonstrate its accuracy by comparing with the standard rectangular finite difference scheme to calculate the electronic response of silicon nanowire solar cells [7–12]. Photonic crystals consisting of such nanowires are promising candidates for solar energy harvesting. We also introduce a radially varying mesh step enabling higher resolution near the radial *pn*-interface.

For angle averaged solar illumination, the absorption profile inside an isolated cylindrical nanowire depends only on the radial coordinate $r$ and vertical $z$ coordinate. In the case of a photonic crystal array of nanowires, light scattering and wave-interference effects give rise to an anisotropic carrier generation profile, determined by the specific symmetries of the photonic crystal. In this case, it is appropriate to expand the drift-diffusion equations (1)–(4) in cylindrical partial waves. In this paper we demonstrate that the cylindrically symmetric partial wave, by itself, provides an accurate description of the short-circuit current and open-circuit voltage of the photonic crystal solar cell.

We start with a brief review of the finite difference scheme in one dimension. The adopted nomenclature is shown in Fig. 1. Mesh nodes are numbered by the index $i$, $x_i$ is the distance from the origin to the $i$-th mesh node, $\Delta x_i = x_{i+1} - x_i$ and $\Delta x_i^{avg} = (\Delta x_i + \Delta x_{i-1})/2$.

The finite difference discretization of (1) is

$$\left(\frac{\psi_{i+1} - \psi_i}{\Delta x_i} - \frac{\psi_i - \psi_{i-1}}{\Delta x_{i-1}}\right) \Big/ \Delta x_i^{avg} = -\frac{q}{\varepsilon}\left(p_i - n_i + N_{D,i} - N_{A,i}\right). \tag{5}$$

* Corresponding author. Tel.: +1 647 832 80 80.
*E-mail address:* deinega@physics.utoronto.ca (A. Deinega).

0010-4655/$ – see front matter © 2012 Elsevier B.V. All rights reserved.
doi:10.1016/j.cpc.2012.05.016


**Fig. 1.** The adopted nomenclature for finite differences. Mesh nodes are numbered by the integer index $i$ (white circles). Discretization of the continuity equation (2) requires approximation of the current at mid-points of the mesh line connecting neighboring nodes (black circles).

The discretization of the the continuity equation for electrons (2) (the continuity equation for holes is treated similarly) is

$$\left(J_n|_{i+1/2} - J_n|_{i-1/2}\right)/\Delta x_i^{avg} = q(R_i - G_i). \tag{6}$$

For evaluation of the current at mid-points of the mesh line (Fig. 1) the Scharfetter–Gummel approximation is commonly used [2]:

$$J_n|_{i+1/2} = qD_n|_{i+1/2}\frac{B(\psi'_{i+1} - \psi'_i)\cdot n_{i+1} - B(\psi'_i - \psi'_{i+1})\cdot n_{i+1}}{\Delta x_i}, \tag{7}$$

where $B(x) = \frac{x}{e^x-1}$, $\psi' = \psi\frac{q}{kT}$, $k$ is Boltzmann's constant, and $T$ is the temperature (the Einstein relation between the diffusion coefficient and the mobility $D = \mu\frac{kT}{q}$ is assumed). This approximation is derived from (3) under the assumption that the electron current density $J_n = J_n|_{i+1/2}$, gradient of the electrostatic potential $\nabla\psi = \frac{\psi_{i+1}-\psi_i}{\Delta x_i}$, and diffusion coefficient $D = D_n|_{i+1/2}$ are constant at $x \in [x_i, x_{i+1}]$, while the electron density $n(x)$ is not constant and satisfies the boundary conditions $n(x_i) = n_i$, $n(x_{i+1}) = n_{i+1}$. This assumption leads to the boundary-value problem (with two boundary values) for the first-order equation

$$J_n|_{i+1/2} = qD_n\frac{\partial n(x)}{\partial x} + q\mu_n n(x)\frac{\psi_{i+1} - \psi_i}{\Delta x_i}, \tag{8}$$

which has a solution

$$n(x) = \left[1 - g(x, \psi')\right]n_i + g(x, \psi')n_{i+1}, \tag{9}$$

$$g(x, \psi') = \frac{1 - \exp\left[\frac{x-x_i}{\Delta x_i}(\psi'_{i+1} - \psi'_i)\right]}{1 - \exp(\psi'_{i+1} - \psi'_i)} \tag{10}$$

if $J_n|_{i+1/2}$ is expressed through the approximation (7). The Scharfetter–Gummel approximation is numerically effective when there are large changes of the carrier concentrations within the computational domain. Using the central finite difference approximation for the concentration and potential derivatives in (3)–(4), on the other hand, can lead to a nonphysical solution unless the mesh resolution is made very high [1]. Since the 1D finite difference scheme can be easily generalized to multi-dimensional systems, we refer to it as a rectangular finite difference in what follows.

Consider now a 2D rotationally symmetric structure. The variables $\psi$, $n$, $p$ can be decomposed into trigonometric Fourier series (partial waves):

$$\psi(r, \varphi) = \sum_{k=0}^{\infty}\psi^k(r)f_k(\varphi), \tag{11}$$

$$n(r, \varphi) = \sum_{k=0}^{\infty}n^k(r)f_k(\varphi), \tag{12}$$

$$p(r, \varphi) = \sum_{k=0}^{\infty}p^k(r)f_k(\varphi), \tag{13}$$

where $r$, $\varphi$ are the usual polar coordinates, $f_0(\varphi) = 1, f_{2k}(\varphi) = \sin k\varphi$ and $f_{2k-1}(\varphi) = \cos k\varphi$, $k = 1, 2, 3\ldots$. The coefficients $\psi^k$, $n^k$ and $p^k$ in (11)–(13) can be considered as components of the vectors $\psi$, $n$, $p$ in the space of trigonometric functions $f_k(\varphi)$.

The angular derivatives can be described by a tensor $\hat{D}$ of order (1, 1) acting in this space:

$$\left(\frac{\partial}{\partial\varphi}\psi\right)^k = \hat{D}^k_{k'}\psi^{k'}. \tag{14}$$

The nonzero elements of this tensor are $\hat{D}^{2k-1}_{2k} = -\hat{D}^{2k}_{2k-1} = k$, $k > 0$, since $\frac{\partial \sin k\varphi}{\partial\varphi} = k\cos k\varphi$ and $\frac{\partial \cos k\varphi}{\partial\varphi} = -k\sin k\varphi$. Here and throughout, the repeated tensor indices are assumed to be summed.

Multiplication of two vectors can be considered as a convolution with tensor $\hat{M}$ of order (1, 2):

$$(\psi n)^k = \hat{M}^k_{l,m}(\psi^l, n^m). \tag{15}$$

This tensor is symmetric with permutation of the last two indices $\hat{M}^k_{l,m} = \hat{M}^k_{m,l}$. The elements of this tensor correspond to well known rules for multiplication of trigonometric functions, for example:
$\hat{M}^0_{1,1} = \hat{M}^3_{1,1} = \frac{1}{2}$, since $\cos\varphi\cos\varphi = \frac{1}{2} + \frac{\cos 2\varphi}{2}$;
$\hat{M}^0_{1,2} = \hat{M}^0_{2,1} = \hat{M}^4_{1,2} = \hat{M}^4_{2,1} = \frac{1}{2}$, since $\sin\varphi\cos\varphi = \frac{1}{2} + \frac{\sin 2\varphi}{2}$.

The system of equations for vectors $\psi$, $n$, $p$ can be obtained by substituting representation (11)–(13) into (1)–(4) with appropriate use of tensors $\hat{D}$, $\hat{M}$, and then projecting the result onto the subspaces corresponding to the functions $f_k(\varphi)$. Discretization of this system leads to a finite difference scheme for the vectors $\psi_i$, $n_i$, $p_i$ defined on the radial mesh. In practice, the Fourier space dimension is limited by some finite number $k_{\max}$.

Here and after superscripts after vectors $\psi$, $n$ and $p$ correspond to their components in the space of trigonometric functions $f_k(\varphi)$, and subscripts correspond to mesh nodes where these vectors are calculated.

Using the Laplacian operator in polar coordinates

$$\nabla^2 = \frac{\partial^2}{\partial r^2} + \frac{1}{r}\frac{\partial}{\partial r} + \frac{1}{r^2}\frac{\partial^2}{\partial\varphi^2} \tag{16}$$

we obtain the finite difference discretization of (1)

$$\left(\frac{\psi_{i+1} - \psi_i}{\Delta r_i} - \frac{\psi_i - \psi_{i-1}}{\Delta r_{i-1}}\right)\Big/\Delta r_i^{avg} + \frac{1}{r_i}\frac{\psi_{i+1} - \psi_{i-1}}{\Delta r_i + \Delta r_{i-1}} + \frac{1}{r_i^2}\hat{D}^2\psi_i = -\frac{q}{\varepsilon}\left(p_i - n_i + N_{D,i} - N_{A,i}\right), \tag{17}$$

where we use the radial coordinate $r$ instead of $x$.

Using the familiar expression for the gradient in polar coordinates

$$\nabla = \frac{\partial}{\partial r}\mathbf{e}_r + \frac{1}{r}\frac{\partial}{\partial\varphi}\mathbf{e}_\varphi \tag{18}$$

leads to the radial and angular components of the electron current density $J_n = J_{n,r}\mathbf{e}_r + J_{n,\varphi}\mathbf{e}_\varphi$:

$$J_{n,r} = qD_n\frac{\partial n}{\partial r} - q\mu_n n\frac{\partial\psi}{\partial r}, \tag{19}$$

$$J_{n,\varphi} = \frac{1}{r}\left(qD_n\frac{\partial n}{\partial\varphi} - q\mu_n n\frac{\partial\psi}{\partial\varphi}\right). \tag{20}$$

Using the divergence of $J_n$ in polar coordinates

$$\nabla\cdot J_n = \left(\frac{\partial}{\partial r} + \frac{1}{r}\right)J_{n,r} + \frac{1}{r}\frac{\partial}{\partial\varphi}J_{n,\varphi}, \tag{21}$$

the finite difference discretization for the continuity equation for electrons (the continuity equation for holes is treated similarly) can be written as

$$\frac{J_{n,r}|_{i+1/2} - J_{n,r}|_{i-1/2}}{\Delta r_i^{avg}} + \frac{1}{r_i}J_{n,r}|_i + \frac{1}{r_i}\hat{D}J_{n,\varphi}|_i = q(R_i - G_i). \tag{22}$$

The components of the recombination vector $R^k$ in (22) can be obtained by numerical projection onto subspaces corresponding to the functions $f_k(\varphi)$

$$R^k = \frac{\int_0^{2\pi} R(r,\varphi) f_k(\varphi) d\varphi}{\int_0^{2\pi} f_k^2(\varphi) d\varphi}, \tag{23}$$

where $R(r,\varphi)$ is calculated using electron and hole concentrations (12), (13) according to common expressions for different types of recombination (radiative, Auger, Shockley–Reed–Hall). Components of the generation vector $G^k$ are obtained in the same way

$$G^k = \frac{\int_0^{2\pi} G(r,\varphi) f_k(\varphi) d\varphi}{\int_0^{2\pi} f_k^2(\varphi) d\varphi}, \tag{24}$$

where $G(r,\varphi)$ is a given generation profile. For a single, isolated, cylindrical nanowire, illuminated by angle-averaged AM1.5 solar radiation, the generation profile is independent on $\varphi$. However, if the nanowires are arranged into a photonic crystal, light scattering and interference effects lead to weak anisotropy in the illumination pattern of each nanowire.

The finite difference expression for the term $J_{n,\varphi}|_i$ in (22) is derived using (20)

$$J_{n,\varphi}|_i = \frac{1}{r_i}\left(qD_n \hat{D} n_i - q\mu_n \hat{M}(n_i, \hat{D}\psi_i)\right). \tag{25}$$

As in the rectangular case, $J_{n,r}|_{i+1/2}$ in (22) is chosen in such a way that the vector equation in the space of trigonometric functions $f_k(\varphi)$

$$J_{n,r}|_{i+1/2} = qD_n \frac{\partial n(r)}{\partial r} - q\mu_n \hat{M}\left(n(r), \frac{\psi_{i+1}-\psi_i}{\Delta r_i}\right) \tag{26}$$

is solvable with some function $n(r)$ defined in the interval $r \in [r_i, r_{i+1}]$, and which satisfies the boundary conditions $n(r_i) = n_i$ and $n(r_{i+1}) = n_{i+1}$. For $k_{\max} = 0$ relation (26) reduces to (8) and can be integrated analytically, giving (7). Otherwise ($k_{\max} > 0$) the value of $J_{n,r}|_{i+1/2}$ can be calculated numerically. $J_{n,r}|_i$ in (22) is obtained as

$$J_{n,r}|_i = \frac{1}{2}(J_{n,r}|_{i+1/2} + J_{n,r}|_{i-1/2}). \tag{27}$$

The above scheme for the Poisson and continuity equations requires modification at the center of coordinates since $r_0 = 0$. In this case we use the rectangular 2D finite difference scheme. For the left hand side of (1) we have for each component $k$

$$\left(\frac{\psi^k_{1,0}-\psi^k_{0,0}}{\Delta x_0} - \frac{\psi^k_{0,0}-\psi^k_{-1,0}}{\Delta x_{-1}}\right) \Big/ \Delta x_0^{avg} + \left(\frac{\psi^k_{0,1}-\psi^k_{0,0}}{\Delta y_0} - \frac{\psi^k_{0,0}-\psi^k_{0,-1}}{\Delta y_{-1}}\right) \Big/ \Delta y_0^{avg}, \tag{28}$$

where the first and second bottom indices correspond to the $x$- and $y$-directions, and $x_0 = y_0 = 0$. Assuming that 2D mesh discretization is symmetric with respect to reflections over $x$ and $y$ axes $x_i = x_{-i} = y_i = y_{-i}$, taking into account the relation between vector components in 2D rectangular mesh and radial 1D mesh (no summation is assumed here) $\psi^k_{i,0} = \psi^k_i f_k(0)$, $\psi^k_{-i,0} = \psi^k_i f_k(\pi)$, $\psi^k_{0,i} = \psi^k_i f_k(\pi/2)$, $\psi^k_{0,-i} = \psi^k_i f_k(3\pi/2)$, and switching to the radial axis $x_i = y_i = r_i$, (28) becomes

$$\frac{1}{\Delta r_0}\left(\frac{\psi^k_1 f_k(0) - \psi^k_0}{\Delta r_0} - \frac{\psi^k_0 - \psi^k_1 f_k(\pi)}{\Delta r_0} + \frac{\psi^k_1 f_k(\pi/2) - \psi^k_0}{\Delta r_0} - \frac{\psi^k_0 - \psi^k_1 f_k(3\pi/2)}{\Delta r_0}\right) = \frac{1}{\Delta r_0^2}\left(\psi^k_1 (f_k(0) + f_k(\pi/2) + f_k(\pi) + f_k(3\pi/2)) - 4\psi^k_0\right). \tag{29}$$

Here and in the next relation (30) we do not imply summation over repeated index $k$.

The discretization of the left part of (2) for each component $k$ can be obtained in a similar way

$$\frac{J_n|^k_{1/2,0} - J_n|^k_{-1/2,0}}{\Delta x_0^{avg}} + \frac{J_n|^k_{0,1/2} - J_n|^k_{0,-1/2}}{\Delta y_0^{avg}} = \frac{J_{n,r}|^k_{1/2}(f_k(0) + f_k(\pi/2) + f_k(\pi) + f_k(3\pi/2))}{\Delta r_0}. \tag{30}$$

If the generation profile is rotationally symmetric, then $R_k(r) = 0$ in (23) for all $k \geq 1$, and we can limit ourselves to $k_{\max} = 0$. As we demonstrate below, this is a good approximation as well, if the generation profile does not vary with the polar angle $\varphi$ significantly. In this case, $k_{\max} = 0$ corresponds to replacing the weakly anisotropic profile with its angular averaged value. The finite difference scheme for this case can be obtained by substituting $\hat{D}^0_0 = 0$, $\hat{M}^0_{0,0} = 1$ into (17), (22):

$$\left(\frac{\psi_{i+1}-\psi_i}{\Delta r_i} - \frac{\psi_i - \psi_{i-1}}{\Delta r_{i-1}}\right) \Big/ \Delta r_i^{avg} + \frac{1}{r_i}\frac{\psi_{i+1}-\psi_{i-1}}{\Delta r_i + \Delta r_{i-1}} = -\frac{q}{\varepsilon}\left(p_i - n_i + N_{D,i} - N_{A,i}\right), \tag{31}$$

$$\frac{J_{n,r}|_{i+1/2} - J_{n,r}|_{i-1/2}}{\Delta r_i^{avg}} + \frac{1}{r_i} J_{n,r}|_i = q(R_i - G_i), \tag{32}$$

where $J_{n,r}|_i$ is calculated using (27). For $J_{n,r}|_{i+1/2}$ we use the Scharfetter–Gummel approximation (7). Since $f_0(\varphi) = 1$, (29) and (30) simplify to

$$4\frac{\psi_1 - \psi_0}{\Delta r_0^2}, \qquad 4\frac{J_n|_{1/2}}{\Delta r_0}. \tag{33}$$

In the following we refer to the scheme defined by (17), (22), (29), (30) as a radial finite difference. Zeroth order radial finite difference scheme corresponds to (31)–(33).

For numerical stability reasons it is more convenient to use the electrostatic potential $\psi$ and quasi-Fermi potentials $\Phi_n$, $\Phi_p$ as independent variables instead of $\psi$, $n$, $p$. The quasi-Fermi potentials are related to $\psi, n, p$ by the following equations:

$$n = n_i \exp\left(\frac{q(\psi - \Phi_n)}{kT}\right), \qquad p = n_i \exp\left(\frac{q(\Phi_p - \psi)}{kT}\right), \tag{34}$$

where $n_i$ is the intrinsic concentration density. In the case of the radial finite difference scheme, we use vector components $\Phi^k_n$, $\Phi^k_p$ that are related to the previously defined $\psi^k$, $n^k$, $p^k$ through

$$n^k = n_i \exp\left(\frac{q(\psi^k - \Phi^k_n)}{kT}\right), \qquad p^k = n_i \exp\left(\frac{q(\psi^k - \Phi^k_p)}{kT}\right). \tag{35}$$

Other numerically efficient transformations are also possible.

For 3D structures with cylindrical symmetry we use radial finite differences (17), (22), (29), (30) for the $r$ and rectangular finite differences (5), (6) for the $z$ directions.

Our approach is benchmarked on a silicon nanowire embedded in silica with length $L = 2\ \mu$m, radius $R = 200$ nm, and distance of the $pn$-interface from the outer side of the nanowire $d = 100$ nm (see Fig. 2, left). The nanowires are arranged in a square lattice photonic crystal with period $a = 800$ nm. As shown later, in this case angular averaging is a good approximation for the solar generation rate, which facilitates use of the zeroth order radial finite difference scheme (31)–(33) with $k_{\max} = 0$.

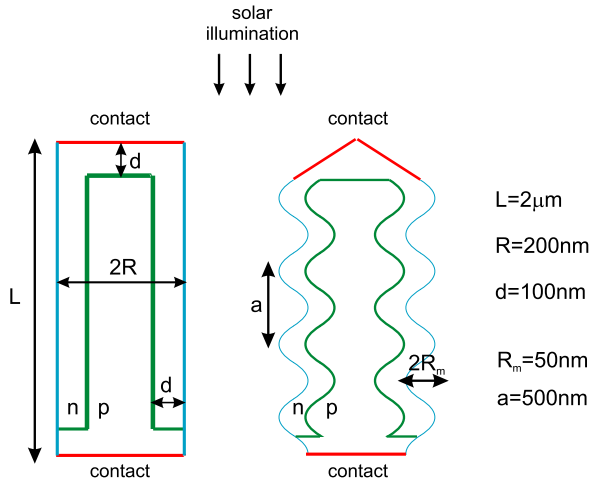


**Fig. 2.** Vertical slices of straight (left) and modulated (right) nanowires. The scale is not preserved. (For interpretation of the references to colour in this figure legend, the reader is referred to the web version of this article.)

In our calculations, we use the silicon parameters found in [7]:

(i) the doping concentration $N_d = N_a = 10^{18}$ cm$^{-3}$,
(ii) the electron and hole mobility $\mu_n = 270$ cm$^2$ V$^{-1}$ s$^{-1}$, $\mu_p = 95$ cm$^2$ V$^{-1}$s$^{-1}$ [13],
(iii) the diffusion coefficient $D_n$, $D_p$ is calculated using the Einstein relation $D = kT\mu/q$ (the temperature $T$ is assumed to be 300 K),
(iv) the surface recombination velocity at the metal contact $S_n = S_p = 10^5$ cm s$^{-1}$.

As in earlier literature [7] we consider only Shockley–Reed–Hall (SRH) recombination from a single-trap level at midgap and choose the lifetime of the minority electrons in the $p$-region equal to the lifetime of the minority holes in the $n$-region ($\tau_{n,\mathrm{SRH}} = \tau_{p,\mathrm{SRH}}$). We use silion with very low minority electron diffusion length $L_n = \sqrt{\tau_{n,\mathrm{SRH}} D_n}$ equal to nanowire radius 200 nm.

We apply the following boundary conditions at the contacts (top and bottom sides of the nanowire):

$$\psi = V_{\mathrm{appl}} + \psi_{\mathrm{bi}}, \tag{36}$$

$$\vec{J}_n \cdot \vec{n} = -qS_n(n - n_0), \tag{37}$$

$$\vec{J}_p \cdot \vec{n} = +qS_p(p - p_0), \tag{38}$$

where $n_0 = \left(\sqrt{(N_D - N_A)^2 + 4n_i^2} + N_D - N_A\right)/2$ and $p_0 = \left(\sqrt{(N_D - N_A)^2 + 4n_i^2} - N_D + N_A\right)/2$ are equilibrium electron and hole concentrations, $V_{\mathrm{appl}}$ is applied voltage (zero at both contacts for the short circuit, zero at the top contact and $V_{oc}$ at the bottom contact for the open circuit), $\psi_{\mathrm{bi}} = \frac{kT}{q}\log(\frac{n_0}{n_i}) = -\frac{kT}{q}\log(\frac{p_0}{n_i})$ is built-in potential, $\vec{n}$ is outer normal to the boundary surface.

At the side surface of the nanowire we apply Neumann boundary conditions

$$\nabla\psi \cdot \vec{n} = 0, \tag{39}$$

$$\nabla n \cdot \vec{n} = 0, \tag{40}$$

$$\nabla p \cdot \vec{n} = 0, \tag{41}$$

that imply no surface charges (the normal component of the electric field is zero) and no current flow through the surface.

Numerical implementation of these conditions is illustrated on the left side of Fig. 3, where the boundary mesh point, B, is

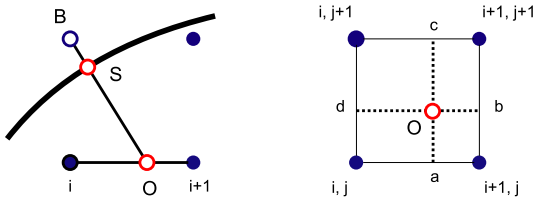


**Fig. 3.** (Left) The boundary mesh point B (empty blue circle) and its nearest internal mesh points (filled circles) separated by the boundary surface. Point S on the surface is the closest one to the boundary point B. Point O is the intersection between the line passing point S and normal to the surface, and the mesh line connecting internal mesh points $i$, $i+1$. (Right) In 3D, point O is located at the mesh plane connecting internal mesh points $(i, j)$, $(i+1, j)$, $(i, j+1)$, $(i+1, j+1)$. (For interpretation of the references to colour in this figure legend, the reader is referred to the web version of this article.)

denoted by an empty blue circle, and the closest mesh points inside the nanowire are denoted by filled circles. To apply the boundary condition (36) we assign the calculated value for $V_{\mathrm{appl}} + \psi_{\mathrm{bi}}$ to the boundary mesh point. Implementation of boundary conditions (37)–(41) requires the following steps (see Fig. 3, left).

(i) Find the point S at the surface which is closest to the boundary point B.
(ii) Draw a line passing point S which is normal to the surface.
(iii) Find the intersection O between this line and the mesh line (in 2D) or mesh plane (in 3D) next to the point B (this mesh line connects the internal points $i$, $i+1$ in Fig. 3, left).
(iv) Find the potential value at the point O by linear interpolation using the values at neighbouring mesh points. In the 2D $(r, z)$ case there are 2 neighbouring mesh points $(i, i+1$ in Fig. 3, left), and the interpolated value is $\psi_O = \frac{x - x_i}{\Delta x_i}\psi_i + \frac{x_{i+1} - x}{\Delta x_i}\psi_{i+1}$. In the 3D $(x, y, z)$ case there are 4 neighbouring points (see Fig. 3, right) and linear interpolation is straightforward.
(v) Find the concentration value at the point O. In 2D we use the Scharfetter–Gummel approximation (9). In 3D we use the following extension of the Scharfetter–Gummel approximation (see Fig. 3, right):
(v.i) calculate the potential (by linear interpolation) and the concentration (by the Scharfetter–Gummel approximation) at the 4 edge points closest to the point O (they are denoted as a, b, c, d in Fig. 3, right) using the values at the mesh points $(i, j)$, $(i+1, j)$, $(i, j+1)$, $(i+1, j+1)$,
(v.ii) calculate the concentration $n_{\mathrm{a-c}}(y)$ (by the Scharfetter–Gummel approximation) in the segment connecting the pair of opposite points a–c, using the values at the points a, c which are calculated according to (v.i),
(v.iii) calculate the concentration $n_{\mathrm{b-d}}(x)$ (by the Scharfetter–Gummel approximation) in the segment connecting the pair of opposite points b–d using values at points the b, d which are calculated according to (v.i),
(v.iv) associate the average $n_{\mathrm{O}} = (n_{\mathrm{a-c}}(y_{\mathrm{O}}) + n_{\mathrm{b-d}}(x_{\mathrm{O}}))/2$ with the corresponding concentration at point O ($x_O$, $y_O$ are the coordinates of O).

With the calculated potential and concentration at the point O we discretize (39)–(41) as $\psi_B = \psi_O$, $n_B = n_O$, $p_B = p_O$.

We discretize (37)–(38) in the following way. For the right hand side of (37)–(38) we use the concentration value at the point B. To estimate the current density in the left hand side of (37)–(38) we take the values of potential and concentration at points B and O and use the Scharfetter–Gummel approximation (7).

The input for the numerical scheme is the charge carrier generation rate from solar illumination which enters the right side of continuity equation (2). To calculate its value, we assume that the nanowires are arranged in a square lattice photonic crystal with period $a = 800$ nm and embedded in silica (refractive index $n = 1.5$) up to their top surface. The photonic crystal

is assumed to sit on a semi-infinite silica substrate with no back-reflector and the region above the structure is air. This architecture is simply chosen to test our numerical method. It is by no means optimized to trap and absorb the maximum amount of sunlight. Electromagnetic calculations are performed using the finite-difference time-domain (FDTD) method [14] with the help of the Electromagnetic Template Library [15]. We assume that the entire solar radiation is collapsed into a normal angle of incidence with linear polarization along the direction connecting neighboring nanowires (oblique incidence case can be simulated with the help of our FDTD iterative technique [16]). We use a subpixel smoothing technique [17] to eliminate the staircase effect caused by the rectangular FDTD mesh. To reduce the numerical reflection from the artificial absorbing perfectly matched layer (PML) [14], we use the additional back absorbing layers technique [18]. Experimental data on the silicon dielectric permittivity $\varepsilon(\omega)$ are taken from [19]. The frequency dependence of $\varepsilon(\omega)$ is assigned in FDTD by considering a modified Lorentz approximation where the dielectric polarization depends both on the electric field and on its first time derivative [20]. This model provides an accurate fit to the response of bulk crystalline silicon to sunlight over the wavelength range from 300 to 1000 nm, while conventional Debye, Drude and Lorentz approximations fail.

We use the standard FDTD scheme, where a plane wave impulse is directed onto the nanowire array, the fields are recorded, transformed to the frequency domain and normalized to the incident spectrum, to calculate the absorption at each point $\mathbf{r}$ inside a nanowire:

$$\alpha(\omega, \mathbf{r}) = \frac{\omega \cdot \mathrm{Im}(\varepsilon)\, |\mathbf{E}(\omega, \mathbf{r})|^2}{c \cdot \mathrm{Re}\left[\mathbf{E}_{inc}(\omega, \mathbf{r}), \mathbf{H}^*_{inc}(\omega, \mathbf{r})\right]}. \tag{42}$$

Here $c$ is the speed of light in vacuum and $\omega$ is frequency of light.

The generation rate $G(\mathbf{r})$ is obtained by integration of the calculated absorption $\alpha(\lambda, \mathbf{r})$ with the incident solar Air Mass 1.5 Global Spectrum [21] intensity $I(\lambda)$ over the wavelength range of 300–1000 nm:

$$G(\mathbf{r}) = \int_{\lambda_{\min}}^{\lambda_{\max}} \frac{\lambda}{hc} I(\lambda)\alpha(\lambda, \mathbf{r}) d\lambda. \tag{43}$$

Here, the wavelength $\lambda = \frac{2\pi c}{\omega}$, $h$ is Planck's constant. We assume that each incident photon of energy $\frac{hc}{\lambda}$ larger than the silicon bandgap leads to the generation of an electron–hole pair. The electrons and holes are assumed to rapidly lose energy by scattering from phonons and occupy energy levels near the conduction and valence band edges, respectively, and are subsequently described by the drift-diffusion equations (1)–(4). The generation rate (43) enters the right side of the continuity equation (2) and is used as an input for the electronic simulations. In Fig. 4 we present typical generation rate cross sectional views for (a) linearly polarized incident light and (b) the noncoherent sum of two perpendicular polarizations. In Fig. 4(c) we present the generation rate profile averaged over the polar angle $\varphi$. Clearly, cross sectional views (b) and (c) differ only slightly from each other. Since solar light is a sum of all possible polarizations, we expect (in agreement with [22]) that the angular averaging

$$G(r, z) = \frac{1}{2\pi} \int_0^{2\pi} G(r\cos\varphi, r\sin\varphi, z) \cdot d\varphi \tag{44}$$

is a good approximation for the solar generation rate $G(r\cos\varphi, r\sin\varphi, z)$. This approximation facilitates use of the zeroth order radial finite difference scheme (31)–(33) with $k_{\max} = 0$.

In Fig. 5 we present the calculated absorption profile $\alpha(\lambda, \mathbf{r})$ for various wavelengths and the total generation rate after angular averaging. The corresponding photocurrent density distribution is

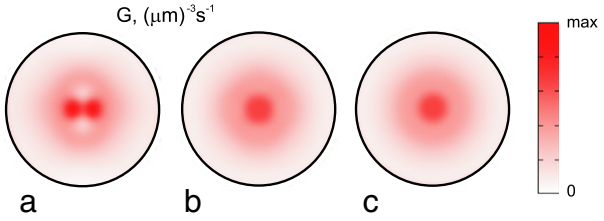


**Fig. 4.** The charge carrier generation rate (43) inside the nanowire (max $= 10^{10}(\mu\mathrm{m})^{-3}\mathrm{s}^{-1}$, linear color bar scale) in cross sectional view at 0.2 μm distance from its top side. (a) The generation rate for linear polarization of the incident light, (b) the generation rate averaged for two perpendicular linear incident polarizations, (c) the angular averaged generation rate. (For interpretation of the references to colour in this figure legend, the reader is referred to the web version of this article.)

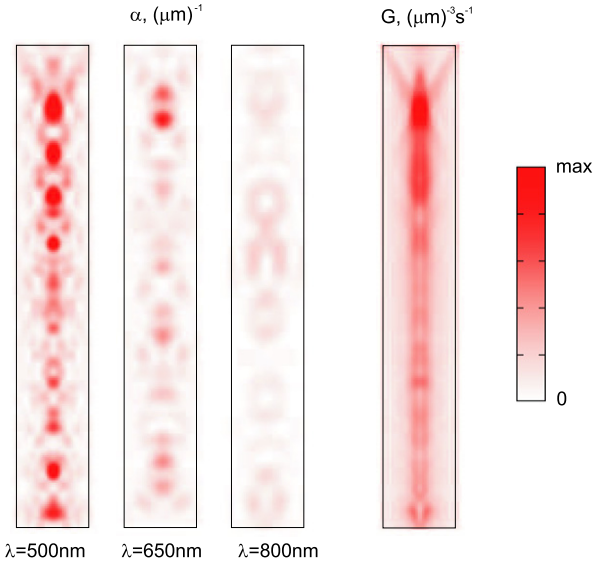


**Fig. 5.** Left, the absorption profile inside the nanowire for the chosen wavelengths (max $= 10\ (\mu\mathrm{m})^{-1}$, linear color bar scale). Right, the corresponding generation rate (43) (max $= 10^{10}\ (\mu\mathrm{m})^{-3}\mathrm{s}^{-1}$). Averaging over the polar angle $\varphi$ is performed. Different scales are used for the vertical and horizontal dimensions. (For interpretation of the references to colour in this figure legend, the reader is referred to the web version of this article.)

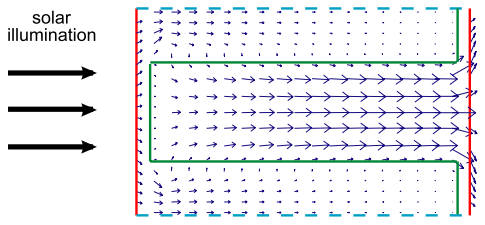


**Fig. 6.** The photocurrent density distribution inside the nanowire (the length of the arrow corresponds to the photocurrent density magnitude). Different scales are used for the vertical and horizontal dimensions. Note that the photocurrent density is higher near the nanowire axis due to the radial geometry.

presented in Fig. 6. The calculated short circuit current density $J_{sc} = 9.48\ \mathrm{mA\ cm}^{-2}$ and the open circuit voltage $V_{oc} = 0.36$ V. The short circuit current density $J_{sc}$ is calculated as the current flux through the contact (bottom or top) normalized on square lattice cell area $a \cdot a$. The electronic calculations were performed in 2D ($r$, $z$) using a mesh step of 0.4 nm.

In Fig. 7 we present an accuracy comparison with the rectangular 3D ($x$, $y$, $z$) finite difference scheme as a function of mesh resolution (due to limited time resources we did not perform 3D calculations with a mesh step smaller than 10 nm). We find that results obtained in 2D ($r$, $z$) using a mesh step of 0.4 nm are

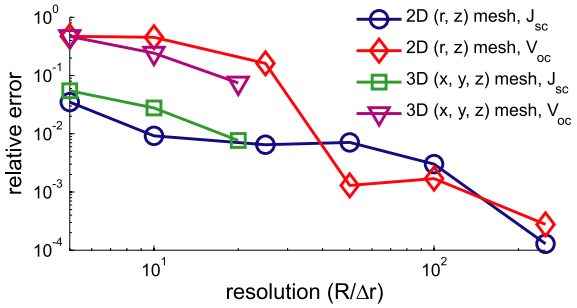


**Fig. 7.** Error in the short circuit current density $J_{sc}$ and open circuit voltage $V_{oc}$ relative to the results $J_{sc}^{ref}$ and $V_{oc}^{ref}$ obtained in the reference case of 2D $(r, z)$ using a mesh step of $\Delta r = 0.4$ nm. A comparison between 2D $(r, z)$ and 3D calculations $(x, y, z)$ (uniform mesh) for the setup in Fig. 2, left and Fig. 5 is presented. The relative errors are calculated as $\frac{|J_{sc}-J_{sc}^{ref}|}{J_{sc}^{ref}}$ and $\frac{|V_{oc}-V_{oc}^{ref}|}{V_{oc}^{ref}}$. The resolution is the ratio between the nanowire radius $R = 200$ nm and $\Delta r$. The considered $\Delta r$ range is 40 nm $\leq \Delta r \leq$ 0.8 nm. The results for $V_{oc}$ are less accurate than those for $J_{sc}$ if the mesh resolution is small.

converged (using a mesh step of 0.8 nm changes the results by less than 0.05%).

The results for $V_{oc}$ demonstrate a larger relative error in comparison with $J_{sc}$ if the resolution is low (insufficiently small mesh spacing). As discussed below, this is primarily caused by the lack of mesh resolution around the *pn*-interface. Clearly, the results for $V_{oc}$ obtained with the radial finite difference $(r, z)$ are less accurate than those obtained with the rectangular finite difference $(x, y, z)$, if the resolution is the same for both cases. This is explained by the fact that first derivatives in (31) and (32) are approximated by central difference with double mesh step. However, the calculations in 3D are much more time consuming than those in 2D. For example, the calculation in 2D with a mesh step of 20 nm is 100 times faster than in 3D (we use the PARDISO [23] library for sparse matrix inversion).

Generally, higher mesh resolution is required around the pn-junction interface since $\psi$, $n$ and $p$ change significantly there. This is easily achieved in 2D $(r, z)$ by varying the mesh step $\Delta r$ in the radial direction (see the top of Fig. 8). This approach cannot be implemented with a 3D $(x, y, z)$ rectangular mesh. However, one can simultaneously use two rectangular meshes with different resolutions (see the bottom of Fig. 8). In the following, we compare results between these two approaches (varying the radial mesh step and using two meshes with different resolutions).

(1) In the first approach (2D, $r, z$, top of Fig. 8) we use:

(i) a small step $\Delta r_s$ close to the *pn*-interface $|r - r_{pn}| < d_{depl}/2$, where $r_{pn} = R - d$ is the position of the *pn*-interface and $d_{depl}$ is the width of the surrounding region that requires higher resolution (we choose $d_{depl} = 40$ nm);

(ii) a large step $\Delta r_l$ far from the *pn*-interface $r < r_{pn} - d_{depl}/2 - w$, $r > r_{pn} + d_{depl}/2 + w$, where $w$ is some control parameter (we put $w = 40$ nm);

(iii) a logarithmically increasing step $\Delta r_s < \Delta r_i < \Delta r_l$ in the intermediate region of width $w$:

$$\Delta r_{i+1} = \alpha \Delta r_i, \quad 1 \leq i < n, \ \alpha > 1 \tag{45}$$

$$\Delta r_1 = \alpha \Delta r_s, \qquad \alpha \Delta r_n = \Delta r_l, \tag{46}$$

$$\sum_{i=1}^{n} \Delta r_i = w. \tag{47}$$

Condition (45) shows that the step $\Delta r_i$ increases logarithmicaly, (46) confines its values to the interval between $\Delta r_s$ and $\Delta r_l$, and (47) ensures that the intermediate region of the width $w$ is completely covered by steps $\Delta r_i$. The parameter $\alpha$ and number of nodes inside the intermediate region $n$ are chosen in order to satisfy these conditions ($n = 3$ for the top of Fig. 8).

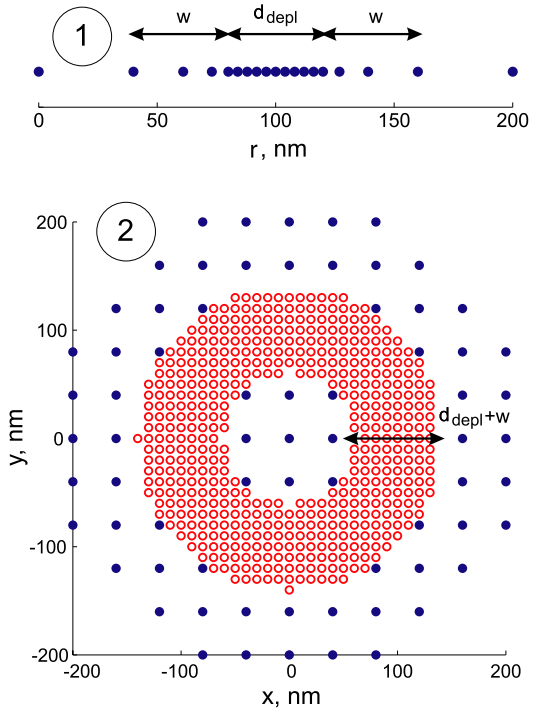


**Fig. 8.** Comparison of nonuniform 2D $(r, z)$ and 3D $(x, y, z)$ meshes, $d_{depl} = 40$ nm, $w = 40$ nm. (1) – Nonuniform step in radial direction, large step $\Delta r_l = 40$ nm, small step $\Delta r_s = 4$ nm. (2) – Covering of calculated volume by two meshes with different resolutions, large step $\Delta x_l = y_l = 40$ nm, small step $\Delta x_s = y_s = 10$ nm. A fine mesh (empty circles) covers the area around the *pn*-interface which is located at the distance $r_{pn} = 100$ nm from the nanowire axis.

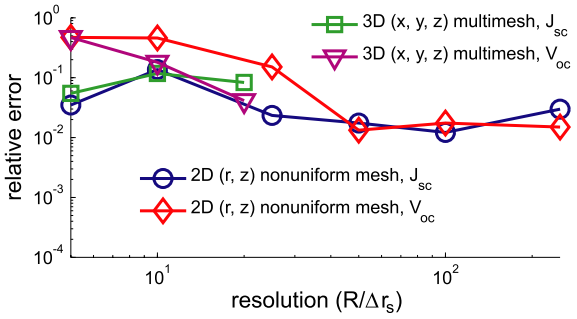


**Fig. 9.** Error relative to the results obtained in 2D $(r, z)$ using the mesh step $\Delta r = 0.4$ nm, comparison between the 2D $(r, z)$ and 3D calculations $(x, y, z)$ using a nonuniform mesh step and a multimesh approach with $\Delta r_l = 40$ nm and varying $\Delta r_s$ (see Fig. 8) for the setup in Fig. 2, left and Fig. 5. The relative error and resolution are calculated as described in the caption to Fig. 7.

(2) In the second approach (3D, $x, y, z$, bottom of Fig. 8) we use:

(i) a fine mesh with a small step $\Delta x_s = \Delta y_s$ at $|r - r_{pn}| < (d_{depl} + w)/2$,

(ii) a rough mesh with a large step $\Delta x_l = \Delta y_l$ at $|r - r_{pn}| \geq (d_{depl} + w)/2$.

Bordering nodes of the rough (fine) mesh use values interpolated by neighboring nodes of the fine (rough) mesh.

A comparison of the accuracy of the two given approaches is presented in Fig. 9 (we use $\Delta r_l = 40$ nm and vary $\Delta r_s$). One can see that decreasing $\Delta r_s$ leads to better results for $V_{oc}$. This is explained by the fact that $V_{oc}$ strongly depends on recombination in the junction area [7], so this area should be covered by a high resolution mesh. The results for $J_{sc}$ initially ($\Delta r_s = \Delta r_l$) show better accuracy than the results for $V_{oc}$. However, an increase of $\Delta r_s$ does not lead to their enhancement. Increase of the mesh resolution

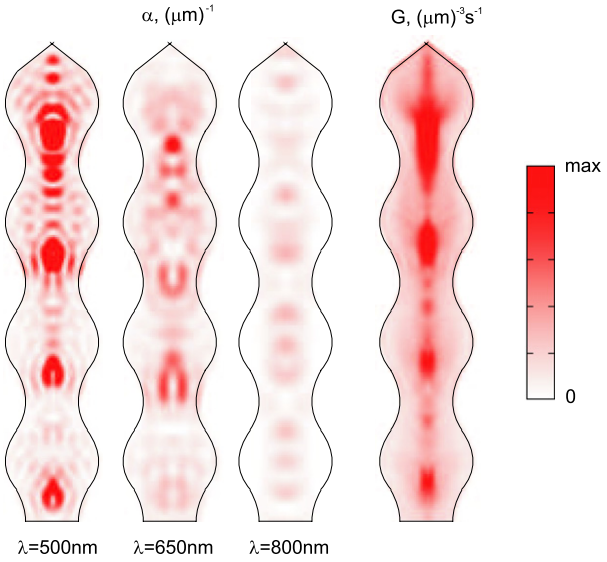


**Fig. 10.** Left, the absorption profile inside a modulated nanowire for chosen wavelengths (max $= 10\ (\mu m)^{-1}$, linear color bar scale). Right, the corresponding generation rate (43) (max $= 10^{10}\ (\mu m)^{-3}s^{-1}$). Averaging over the polar angle $\varphi$ is performed. Different scales are used for the vertical and horizontal dimensions. (For interpretation of the references to colour in this figure legend, the reader is referred to the web version of this article.)

throughout the structure is necessary to obtain better results for $J_{sc}$ since photocurrent is generated throughout the whole nanowire.

Finally, we demonstrate the accuracy of the radial finite difference scheme for sinusoidaly modulated nanowires (see Fig. 2, right). Such modulation can lead to strong light trapping effects due to the phenomenon of parallel interface refraction (PIR) [24]. The radius of the nanowires depends on $z$ as

$$R(z) = R - R_m \cos(2\pi z/a_z), \quad z \geq a_z/4, \tag{48}$$

$$R(z) = \frac{z}{a_z/4} R, \quad z < a_z/4, \tag{49}$$

where $R_m$ is the amplitude of the modulation and $a_z$ is the lattice constant along the $z$ direction ($z = 0$ corresponds to the top of the nanowire, and $z = L$ to the bottom of the nanowire). The cone shape of the nanowire near the top can serve as an anti-reflection layer for incoming sunlight, since it provides a gradual change of the effective dielectric permittivity [25]. The modulation of the *pn*-interface follows the surface modulation as shown by the green line in Fig. 2, right. For our calculations we use $R_m = 50$ nm, $a_z = 500$ nm and all other parameters are the same as considered above for straight nanowires. In Fig. 10 we present the absorption profile $\alpha(\lambda, \mathbf{r})$ for various wavelengths and the integrated generation rate after angular averaging (43). The calculated short circuit current density $J_{sc} = 14.6\ \text{mA cm}^{-2}$ and the open circuit voltage $V_{oc} = 0.377$ V. The calculations are performed in 2D $(r, z)$ using a mesh step of 0.4 nm.

In Fig. 11 we present an accuracy comparison with the rectangular 3D $(x, y, z)$ finite difference scheme. The results obtained in 2D $(r, z)$ using a mesh step of 0.4 nm are found to be converged (using a mesh step of 0.8 nm changes the results by less than 0.1%). The relative error for $J_{sc}$ and $V_{oc}$ is larger than that for straight nanowires, especially if the mesh resolution is small (compare Figs. 7 and 11), since the surface of the modulated nanowire is not aligned with the $z$ mesh direction. To accurately account for the curvature of the surface, a higher mesh resolution is needed. The corresponding 3D calculations are time consuming and cumbersome.

In summary, we have demonstrated the effectiveness of a partial-wave finite difference discretization of the semiconductor

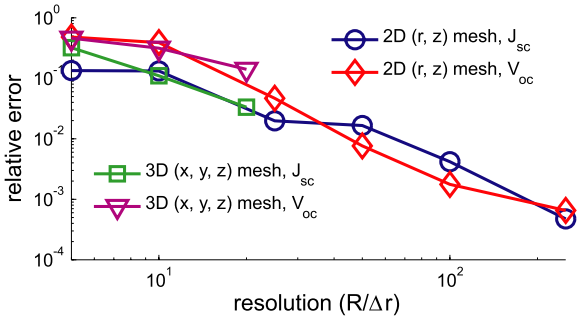


**Fig. 11.** The error relative to the results obtained in 2D $(r, z)$ using a mesh step of $\Delta r = 0.4$ nm, comparison between 2D $(r, z)$ and 3D calculations $(x, y, z)$ for the setup in Fig. 2, right and Fig. 10 (nanowire with radius modulation along the vertical axis). The relative error and resolution are calculated as described in the caption to Fig. 7.

drift-diffusion equations for cylindrically symmetric structures with radial *pn*-junction geometry. In the case of a photonic crystal that breaks the cylindrical symmetry in the optical absorption profile, we found that the lowest order (rotationally symmetric) partial-wave provides accurate results for both the short circuit current and the open circuit voltage. We compared our results with the accuracy of a standard rectangular finite difference scheme in order to verify that our proposed scheme is suitable for describing the electronic properties of nanowire photonic crystal solar cells. Our illustrated structures were not optimized to achieve the maximum solar cell efficiency. Suitably optimized photonic crystal nanowire arrays are expected [26] to achieve short circuit current densities $J_{sc}$ of the order of 30 mA cm$^{-2}$ using an effective bulk thickness of 1 μm of crystalline silicon.

## Acknowledgments

This work is supported in part by the United States Department of Energy contract DE-FG02-10ER46754, the Natural Sciences and Engineering Research Council of Canada, and the Canadian Institute for Advanced Research.

## References

[1] D. Vasileska, S.M. Goodnick, Computational Electronics, Morgan and Claypool, 2006.
[2] S. Selberherr, Analysis and Simulation of Semiconductor Devices, Springer, Springer-Verlag, Wien New York, 1984.
[3] R. Kircher, W. Bergner, Three-Dimensional Simulation of Semiconductor Devices, Birkhauser Verlag, 1991.
[4] A. Franz, G. Franz, S. Selberherr, C. Ringhofer, P. Markowich, Finite boxes – A generalization of the finite difference method suitable for semiconductor device simulation, IEEE Trans. Electron Devices ED-30 (9) (1983) 1070–1082.
[5] K. Matsumoto, I. Takayanagi, T. Nakamura, R. Ohta, The operation mechanism of a charge modulation device (CMD) image sensor, IEEE Trans. Electron Devices 38 (5) (1991) 989–998.
[6] M. Spevak, T. Grasser, Discretization of macroscopic transport equations on non-Cartesian coordinate systems, IEEE Trans. CAD Integr. Circuits Syst. 26 (8) (2007) 1408–1416.
[7] B.M. Kayes, H.A. Atwater, N.S. Lewis, Comparison of the device physics principles of planar and radial p–n junction nanorod solar cells, J. Appl. Phys. 97 (2005) 114302.
[8] R. Kapadia, Z. Fan, A. Javey, Design constraints and guidelines for CdS/CdTe nanopillar based photovoltaics, Appl. Phys. Lett. 96 (2010) 103116.
[9] L. Tsakalakos, J. Balch, J. Fronheiser, B.A. Korevaar, O. Sulima, J. Rand, Silicon nanowire solar cells, Appl. Phys. Lett. 91 (2007) 233117.
[10] L. Hu, G. Chen, Analysis of optical absorption in silicon nanowire arrays for photovoltaic applications, Nano Lett. 7 (11) (2007) 3249.
[11] Z. Fan, H. Razavi, J. Do, A. Moriwaki, O. Ergen, Y.-L. Chueh, P.W. Leu, J.C. Ho, T. Takahashi, L.A. Reichertz, S. Neale, K. Yu, M. Wu, J.W. Ager, A. Javey, Three dimensional nanopillar array photovoltaics on low cost and flexible substrates, Nature Materials 8 (2009) 648.
[12] J.S. Li, H.Y. Yu, S.M. Wong, X.C. Li, G. Zhang, P.G.Q. Lo, D.L. Kwong, Design guidelines of periodic Si nanowire arrays for solar cell application, Appl. Phys. Lett. 95 (2009) 243113.
[13] http://www.ioffe.rssi.ru/SVA/NSM/Semicond/Si/electric.html.
[14] A. Taflove, S.H. Hagness, Computational Electrodynamics: The Finite Difference Time-Domain Method, Artech House, Boston, 2005.
[15] Electromagnetic Template Library (EMTL), Kintech Lab Ltd, http://fdtd.kintechlab.com.

[16] I. Valuev, A. Deinega, S. Belousov, Iterative technique for analysis of periodic structures at oblique incidence in the finite-difference time-domain method, Opt. Lett. 33 (2008) 1491–1493.
[17] A. Deinega, I. Valuev, Subpixel smoothing for conductive and dispersive media in the FDTD method, Opt. Lett. 32 (2007) 3429–3431.
[18] A. Deinega, I. Valuev, Long-time behavior of PML absorbing boundaries for layered periodic structures, Comput. Phys. Comm. 182 (2011) 149–151.
[19] M.A. Green, M. Keevers, Optical properties of intrinsic silicon at 300 K, Prog. Photovolt. 3 (1995) 189–192.
[20] A. Deinega, S. John, Effective optical response of silicon to sunlight in the finite-difference time-domain method, Opt. Lett. 37 (2012) 112–114.
[21] http://rredc.nrel.gov/solar/spectra/am1.5.
[22] M.D. Kelzenberg, M.C. Putnam, D.B. Turner-Evans, N.S. Lewis, H.A. Atwater, Predicted efficiency of Si wire array solar cells, in: Proceedings of the 34th IEEE PVSC, 2009.
[23] PARDISO, http://www.pardiso-project.org.
[24] A. Chutinan, S. John, Light trapping and absorption optimization in certain thin-film photonic crystal architectures, Phys. Rev. A 78 (2008) 023825.
[25] A. Deinega, I. Valuev, B. Potapkin, Yu. Lozovik, Minimizing light reflection from dielectric textured surfaces, JOSA A 28 (5) (2011) 770–777.
[26] G. Demesy, S. John, Solar energy trapping with modulated silicon nanowire photonic crystals, J. Appl. Phys. (in press).